High-frequency sea-level extremes: Global correlations to synoptic atmospheric patterns

Petra Zemunik [a,*], Cléa Denamiel [b], Joanne Williams [c], Ivica Vilibić [b]

[a] *Institute of Oceanography and Fisheries, Šetalište I. Meštrovića 63, 21000, Split, Croatia*
[b] *Ruđer Bošković Institute, Division for Marine and Environmental Research, Bijenička Cesta 54, 10000, Zagreb, Croatia*
[c] *National Oceanography Centre, 6 Brownlow Street, Liverpool, L3 5DA, UK*

ARTICLE INFO

ABSTRACT

With the increase of available global observations at a minute resolution, emerging studies of high-frequency sea-level oscillations have already produced climatologies and explored the atmospheric processes driving the related flooding events, in a qualitative manner and/or at a very local scale. In the presented work, however, the global connections between nonseismic sea-level oscillations at tsunami timescales (NSLOTTs) and synoptic patterns are quantified for 307 tide gauge sites around the world. A global index, constructed for each site over the whole data interval as the linear combination of a prescribed set of synoptic variables extracted from the ERA5 atmospheric reanalysis, is correlated with hourly-averaged NSLOTTs. The correlation between this index and the NSLOTT ranges varies between sites but is generally higher at mid-latitudes and particularly in the Mediterranean Sea where correlations reach 0.8. Mid-troposphere wind speed is found to be the best correlated synoptic variable at roughly one third of all sites together with the mid-troposphere relative humidity. Consequently, wave-ducting is believed to be the dominant mechanism for the NSLOTT propagation and longevity. For such conditions, extreme NSLOTT events are accompanied, on average, by a very specific synoptic pattern including mid-troposphere jet streams, low-troposphere thermal fronts and poleward surface cyclones, independently of the hemisphere or the site and despite some differences in intensity. Following this study, in regions with high correlations, various applications of the index - from climate studies to operational forecasts - could lead to a broader understanding of the NSLOTT events around the world.

1. Introduction

The science related to atmospherically-induced high-frequency sea-level oscillations, and their extreme manifestations known as meteorological tsunamis or meteotsunamis (the term is introduced by Nomitsu, 1935), have been developed in the previous century. At its beginnings, it was mainly focusing on explaining and describing the isolated destructive events causing coastal flooding, structural damages and/or human casualties. Following the advances made in global and systematic observational research, two review papers by Rabinovich and Monserrat (1996, 1998) popularized the term meteotsunami at the end of the 1990s, but basin-wide and global climatology studies only started less than a decade ago (Šepić et al., 2015a; Bechle et al., 2016; Vilibić and Šepić, 2017; Dusek et al., 2019; Kim et al., 2021).

Recently, the concept of nonseismic sea-level oscillations at tsunami timescales (NSLOTTs) – that generalizes the research on meteotsunamis

to all atmospherically-induced high-frequency oscillations – was introduced by Vilibić and Šepić (2017). In their initial global study, they found 99% significant correlation between zonally averaged winds at 500 hPa and NSLOTT ranges. This demonstrates the importance of mid-troposphere jet streams in generating NSLOTT events. Such a synoptic condition is also a well-known meteotsunamigenic pattern which was recorded during meteotsunami events occurring in the USA (Thomson et al., 2009; Šepić and Rabinovich, 2014; Rabinovich et al., 2021), in the Mediterranean Sea (Jansà et al., 2007; Vilibić and Šepić, 2009; Šepić et al., 2012, 2015b; Jansà and Ramis, 2021; Zemunik et al., 2021a), in the northeast Atlantic basin (Tappin et al., 2013; Sibley et al., 2016) and in Japan (Tanaka, 2010). Aside from anomalously strong upper-layer winds, other atmospheric patterns are also known to be critical for NSLOTT and meteotsunami generation, including: (i) an inflow of warm and dry air in the lower troposphere, (ii) instability of the mid-troposphere, (iii) weak surface cyclone, and (iv) winds that

---

increase from the surface towards the upper levels. However, in some regions of the world, NSLOTT events may be accompanied by other atmospheric patterns, presumably depending on the atmospheric processes driving the meteotsunamigenic disturbances.

Connecting NSLOTTs to atmospheric processes for the purpose of detection of meteotsunami events (i.e., linking specific combination of synoptic patterns to destructive event) is thus of the outmost importance. However, till now, it has only been successfully implemented in Ciutadella (Balearic Islands), a known meteotsunami "hot spot" where several studies have demonstrated the potential of such an approach. The very first application was based on a qualitative assessment of the synoptic conditions applied to the forecast of meteotsunami events within the Balearic rissaga warning system – the oldest, and still operational, meteotsunami early warning system (Ramis and Jansà, 1983; Jansà and Ramis, 2021). Later, Šepić et al. (2016) used atmospheric reanalyses to reconstruct the past NSLOTT events with a synoptic meteotsunami index, while Vilibić et al. (2018) applied this index to estimate the far-future NSLOTT events and derive meteotsunami hazard in Ciutadella based on regional climate models. Further, these studies suggested that such an index could be created for any other location in the world where long-term records of high-frequency sea-levels exist and for which synoptic patters are strongly correlated with NSLOTTs.

With the recent creation of the Minute Sea-Level Analysis (MISELA) dataset (Zemunik et al., 2021b) compiling global NSLOTTs records and the release of the hourly ERA5 atmospheric reanalyses (Hersbach et al., 2020), studying the link between NSLOTTs and atmospheric processes worldwide became possible. Therefore, this study – which complements the research of Zemunik et al. (2022) where global distributions, spectral properties and coherence patterns of NSLOTTs were examined – aims to demonstrate that the connection between synoptic settings and NSLOTTs can be established in the world oceans. A global NSLOTT index was thus constructed, individually at each of the 307 world locations extracted from the MISELA dataset, with the optimal combination of synoptic variables describing the atmospheric setup above each area during moderate and pronounced NSLOTTs.

The structure of this article is as follows. In Section 2, the data and methods used in the analyses, and for the definition of the NSLOTT index, are presented. Section 3 describes the synoptic variables and their connection with the NSLOTTs, while Section 4 illustrates the atmospheric setup during extreme NSLOTTs. In Section 5, the construction of the NSLOTT index using the most relevant variables is described and its distribution across the world's coastlines is presented. Finally, Section 6 provides a detailed discussion of the results, while the main conclusions of the study are presented in the last section.

2. Data and methods

2.1. MISELA dataset

All the presented analyses are based on the MISELA dataset (Zemunik et al., 2021c) which contains 1-min sea-level data from 331 tide gauges worldwide. This dataset has been developed to enable global and regional research of short-period (T < 2 h) sea-level oscillations with atmospheric origin. Most of the data originate from the Intergovernmental Oceanographic Commission Sea Level Station Monitoring Facility (IOC SLSMF, http://www.ioc-sealevelmonitoring.org). The data have passed through several steps of quality-control procedure in order to obtain research-quality product and have been filtered to extract the high-frequency oscillations only. What distinguishes the MISELA dataset from other available sea-level datasets is threefold. First, the quality-controlled high-frequency sea-level data are available for the global tide gauges, whereas other available datasets provide either global coverage of lower-frequency data (e.g. Global Extreme Sea-Level Analysis, GESLA, Haigh et al., 2022; Permanent Service for Mean Sea Level, PSMSL, Holgate et al., 2013) or only regional coverage of high-frequency data (e.g. NOAA Tides and Currents dataset, https

://tidesandcurrents.noaa.gov). Second, manual procedures have been introduced due to the great amount of data unable to reach high quality using automatized quality-control procedures only. Third, records of seismic tsunamis have been excluded using global tsunami catalogues and the data have been filtered with 2-h Kaiser-Bessel filter which both eliminated some problems in the data (e.g. shifts and drifts) and extracted the high-frequency signal needed to investigate atmospherically-induced short-period processes such as seiches, meteotsunamis, infragravity and coastal waves. For a detailed explanation of the dataset and quality control procedure see Zemunik et al. (2021b).

Following the methodology described by Zemunik et al. (2022), data flagged as interpolated in the MISELA dataset were excluded from the series, except when the interpolation was done for segments of 5 min or less (removing those data would leave series overly interrupted with data-gaps). Moreover, hourly data sequences attached to the gaps and data sequences shorter than 6 h in between the gaps were also removed, as some methods (e.g., filtering) are considered inaccurate at the borders of a data series. From each NSLOTT series, the range of oscillations was calculated by estimating the Euclidean distance between the upper and lower envelope of the series in each minute. Envelopes are boundaries within which the signal is contained, constructed by spline interpolation over local extrema (Fig. 2a). In this analysis, envelopes were estimated by using the MATLAB function *envelope* (Cook et al., 2015). As the ERA5 atmospheric data used in this work have an hourly coverage, the sea-level ranges (estimated as distances between the envelopes) were then averaged to an hourly timescale to allow for reliable quantification of connection between the atmospheric setup and the high-frequency sea-level processes (Fig. 2b). Practically, the hourly average is calculated for a time interval 29 min before and 30 min after each full hour, considering only hourly windows which have at least 50% of the data. Taking hourly averages of the NSLOTT ranges reduced the maximal range in an hourly window by 30% on average. However, methods (like correlation analysis) used in this study are almost insensitive to the changes of data scale, yet some downsides of averaging exist because intervals that have changing NSLOTT ranges are more influenced by taking an hourly average than those having homogenous values of ranges.

For the analysis of the pronounced NSLOTTs, ten most extreme NSLOTT events have been selected at each station in order to analyse an average synoptic situation during these events. Extreme NSLOTT events are chosen by the following criteria: they must have a maximum 24-h variance, contain no more than 10% of data-gaps and not overlap between each other. At the end, 24 stations from the MISELA dataset were excluded from the analysis, as not fulfilling these criteria or having some odd behaviours in the spectra (e.g., aliasing) which signalled potential problems in the data (Zemunik et al., 2022). Therefore, in total time-series from 307 stations were used in the analysis and their distributions in space and length are shown in Fig. 1.

2.2. ERA5 synoptic variables

In this study, for each of the 307 NSLOTT records, specific synoptic conditions were extracted from the European Centre for Medium-range Weather Forecast (ECMWF) ERA5 reanalysis dataset (Hersbach et al., 2020, https://www.ecmwf.int/en/forecasts/datasets/reanalysis-datasets/era5). The hourly ERA5 dataset has a spatial resolution of approximately 30 km and resolves the atmosphere for 137 vertical levels from the surface up to a height of 80 km. Hereafter, only wind speed, relative humidity and geopotential, temperature and mean sea-level pressure were used, as these specific variables are known to be relevant for the connection of meteotsunamis and NSLOTT events to synoptic patterns (Šepić et al., 2015a, 2016).

The ERA5 atmospheric fields were extracted for the period of activity (entire length of time series) of each tide gauge station. The considered fields are: (1) vertical profiles of wind speed, temperature and relative
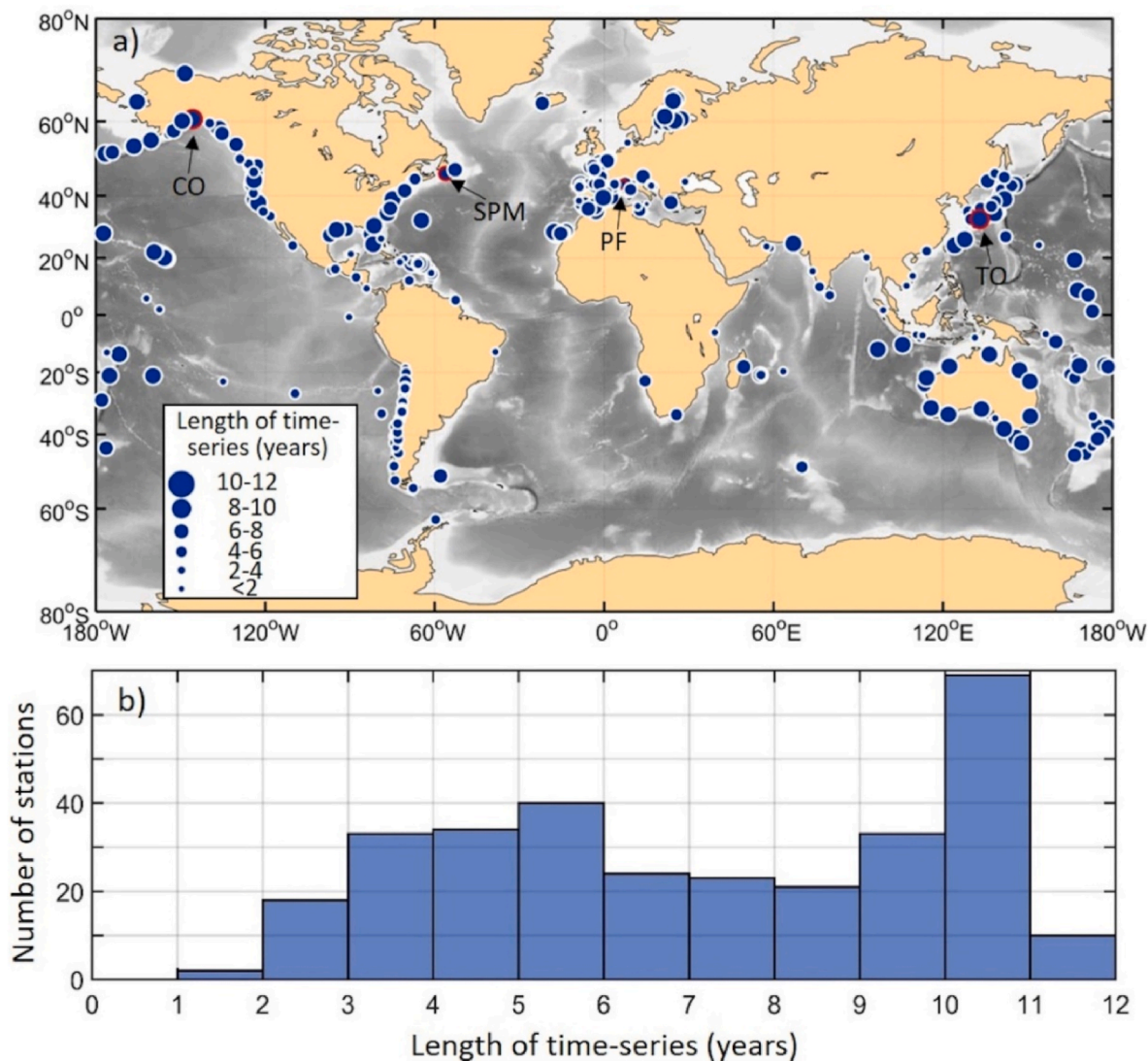
Fig. 1. a) Locations of the tide gauge stations from the MISELA dataset used in the analysis, and b) distribution of the length of time-series. Black arrows point to 4 stations used in Section 5: (i) Cordova, US (CO), (ii) Saint Pierre et Miquelon, France, northwest Atlantic Ocean (SPM), (iii) Port Ferréol, France (PF), and (iv) Tosashimizu, Japan (TO).

humidity from the surface up to a pressure level of 400 hPa at the ERA5 grid point closest to the corresponding tide gauge, and (2) horizontal fields of mean sea-level pressure, temperature at 850 hPa and geopotential at 550 hPa in a rectangular area 10° in each cardinal direction from a centre, which is a grid point closest to the tide gauge (Table 1). Correlations between entire time series of synoptic variables and hourly NSLOTT ranges at simultaneous times are estimated to find the most relevant variables and variable combinations used for construction of NSLOTT index. For each of the synoptic variable listed in (1) the values at all pressure levels in the middle (400–700 hPa) or lower (800–950 hPa) troposphere (with 25–50 hPa step) above each tide gauge station were considered, as well as the vertical gradient of values at different pressure levels. For horizontal fields of variables listed in (2), differences between values at the point closest to the tide gauge and each point in the rectangular area around the tide-gauge (with 0.25° step) have been calculated. Finally, those variables that obtained highest correlation with the NSLOTT ranges at a tide gauge station have been retained for further analyses and construction of the NSLOTT index.

2.3. Construction of the NSLOTT index

To construct the global NSLOTT index, at each of the 307 stations, the atmospheric synoptic variables from Table 1 presenting the highest correlations with the hourly NSLOTT ranges were linearly combined as follows:

$$\mu_n(t) = \sum_{i=1}^{n} \alpha_i x_i(t) ,$$

with $n \in [1,7]$ the number of synoptic variables (from Table 1) used in the construction of the index μ_n, x_i the synoptic variable, α_i the corresponding coefficient and t the time. To construct the index μ_1 (i.e., for $n = 1$), the synoptic variable that obtained the highest absolute correlation with the NSLOTT time series was selected for the choice of x_1. The variable is chosen individually for each station. The coefficient α_1 is estimated as the solution of the system of equations $h(t) = \mu_1(t)$ using the least square method, where h is the hourly NSLOTT range. Next, to construct μ_2, the first synoptic variable x_1 was adopted from μ_1, while the second synoptic variable x_2 was selected using the cost function. The cost function was calculated for each of the remaining synoptic variables
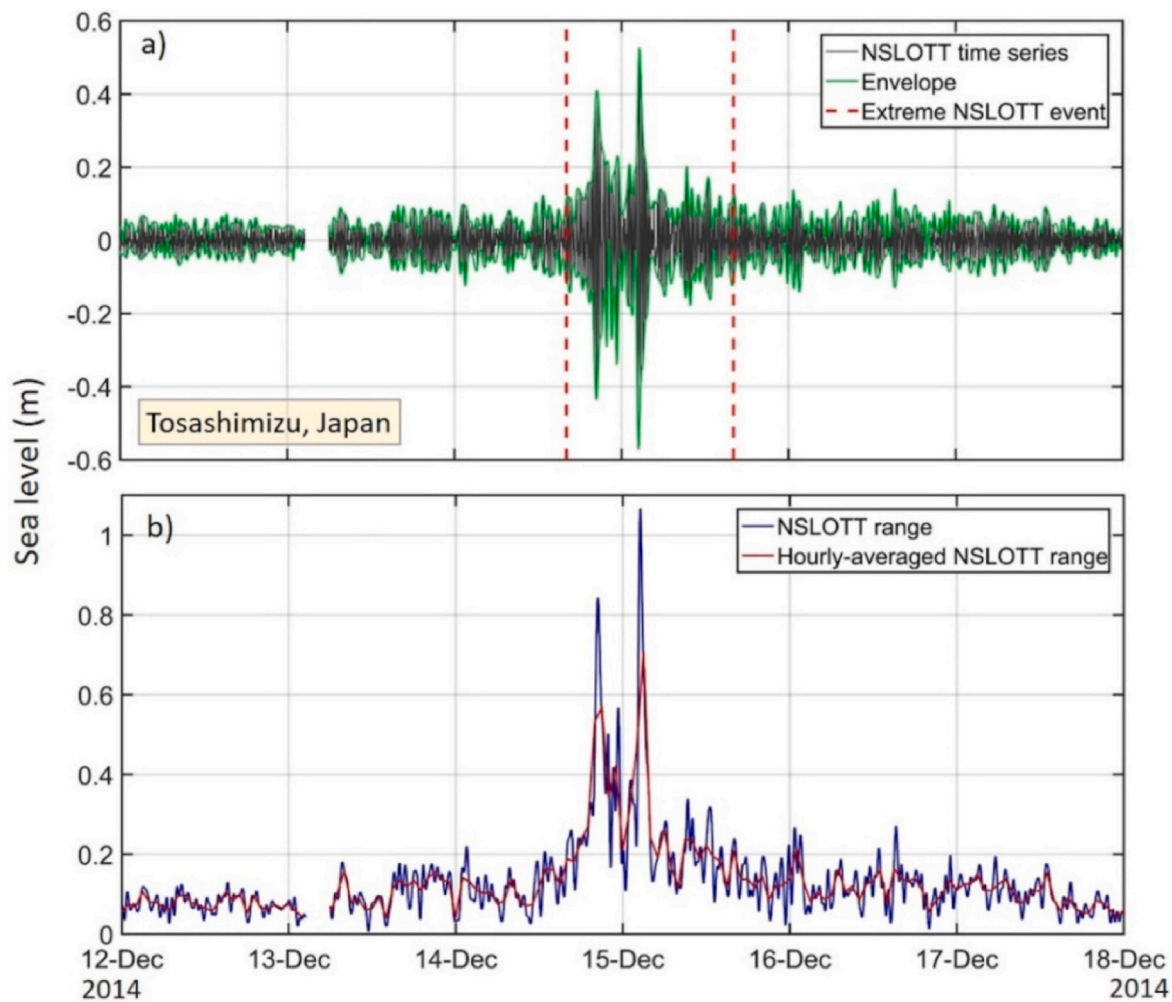
Fig. 2. a) An example of NSLOTT series (station Tosashimizu, Japan, period 12–18 December 2014) with upper and lower envelope used for estimation of sea-level range, and b) sea-level ranges during same period and its hourly averages used for estimation of correlations with synoptic variables.

Table 1
The list of ERA5 synoptic variables used in analysis and their features.

Vertical profiles			Horizontal (spatial) fields		
Synoptic variable	Height	Value/ gradient	Synoptic variable	Height	Value/ gradient
Wind speed	Mid-troposphere (400–700 hPa)	Value	Geopotential	550 hPa	Gradient (step 0.25°)
	Surface	Value	Mean sea-level pressure	Surface	Gradient (step 0.25°)
Relative humidity	Mid-troposphere (400–700 hPa)	Value	Temperature	850 hPa	Gradient (step 0.25°)
Temperature	Low-troposphere (800–950 hPa)	Gradient (step 50 hPa)			

as the correlation between the selected variable and the NSLOTT time series minus the correlation between that same variable and the x_1. The variable with the highest cost function has been chosen for x_2, again for each station individually. Having the x_2, the coefficient α_2 is estimated as the solution of the system $h(t) = \mu_2(t)$. Analogously, the index μ_3 was created having the same synoptic variables x_1 and x_2 as μ_2, while

choosing for x_3 a variable that has the highest cost function, i.e. a sum of costs relative to x_1 and x_2 (calculated as described for μ_2). Following this procedure, indices μ_4 to μ_7 have been created, too.

Finally, for each station, an optimal index μ was chosen (hereafter referred as the NSLOTT index). Namely, μ_n is considered optimal if the correlation between μ_{n+1} and h is not at least 0.01 higher than the correlation between μ_n and h, i.e., if adding a new variable is not substantially increasing correlations between the NSLOTT index and the hourly NSLOTT range. In the end, each station can have between 1 and 7 synoptic variables in the optimal index, chosen among the variables from Table 1 and in the specific order as defined by this procedure. Construction of the NSLOTT index is illustrated in Fig. 3.

3. Connection between NSLOTT and synoptic variables

In this section, the correlations between synoptic variables and NSLOTT ranges are investigated at each of the 307 stations to extract common behaviours at the global scale. The correlations are estimated over the whole interval on which sea level data is available. First, the maximum correlation coefficient between the NSLOTT range recorded at each tide-gauge station and the vertical synoptic variables at pressure levels at the point closest to the tide gauge are presented in Figs. 4 and 5. The correlation with the mid-troposphere wind speed is positive almost everywhere, varies from weak to strong and spans between −0.45 and 0.65, with the median of 0.27 (Fig. 4). It should be highlighted that the correlation significance threshold is relatively low, as correlations are
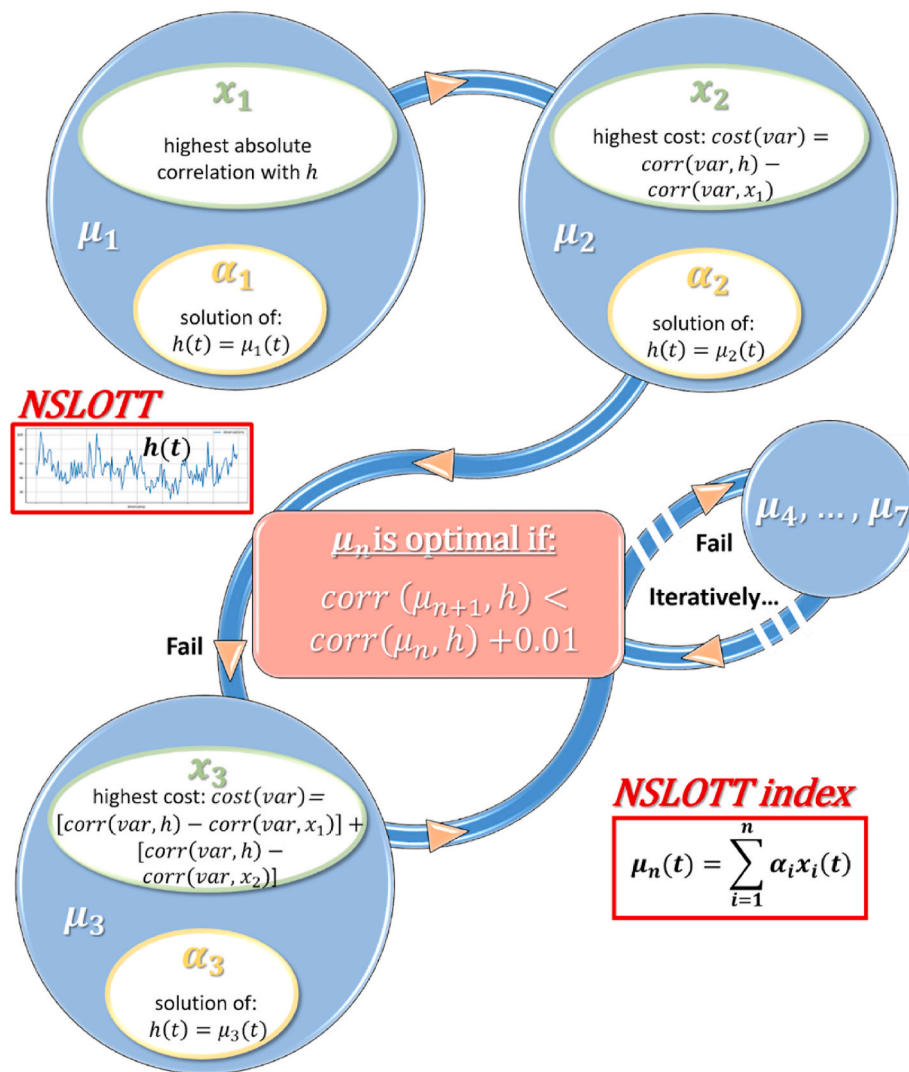
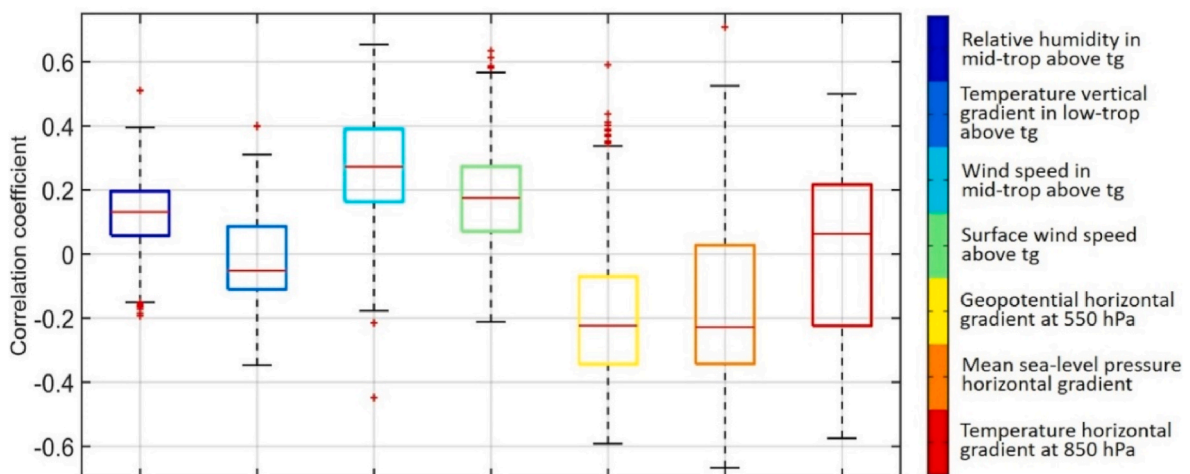**Fig. 3.** A diagram of construction of the NSLOTT index.

Fig. 4. Boxplots of the correlation coefficient between the NSLOTT range and each synoptic variable. On each boxplot, the central red mark indicates the median, and the bottom and top edges of the box indicate the 25th and 75th percentiles, respectively. The whiskers extend to the lowest and highest values (not considered as outliers), and the outliers are shown as red pluses. In the legend "tg" stands for tide gauge and "trop" stands for troposphere. (For interpretation of the references to colour in this figure legend, the reader is referred to the Web version of this article.)
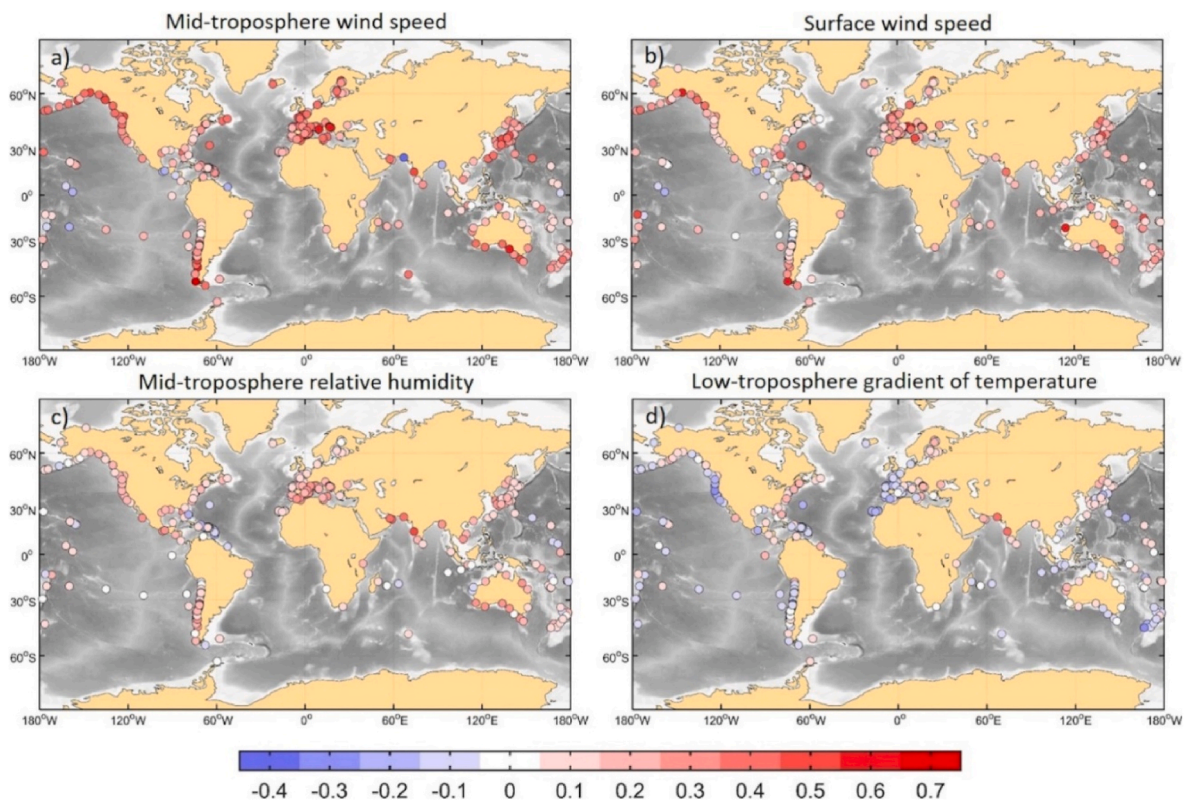
Fig. 5. World map of maximum correlation coefficient between the NSLOTT range and a) mid-troposphere wind speed, b) surface wind speed, c) mid-troposphere relative humidity, and d) low-troposphere vertical gradient in temperature above each tide-gauge station.

based on a large amount of data. For example, for 17 500 data in a sea-level series which is around two-years long, the correlation of 0.02 is already significant at 99%. The highest correlation with the mid-troposphere wind speed is obtained in the regions of the Mediterranean, Northern Europe, Western Japan, Southern Australia, North-west America and Southern Chile, while being lowest and even negative in the tropics (Fig. 5a). A spatial global pattern is thus suggested by this analysis: correlations are increasing towards the mid-latitudes, where mid-troposphere winds are persistent and known to co-occur with NSLOTTs, unlike tropical regions which have lower correlations due to the absence of mid-troposphere jets. This is aligned with the fact that the wind is recognized as a key synoptic feature for generation and longevity of meteotsunami and NSLOTT disturbances (Šepić et al., 2015b; Vilibić and Šepić, 2017). Moreover, mid-troposphere wind jets are weaker in the tropical belt (Lee, 1999) where NSLOTTs have much lower ranges and do not usually reach extreme values (Zemunik et al., 2022).

The correlation with the surface wind speed is somewhat weaker, between −0.21 and 0.63, with the median of 0.17. The correlations are lower than for the mid-troposphere wind speed, but have similar spatial distribution (Fig. 5b). The next variable is relative humidity in the mid-troposphere, describing the stability of the jet stream, with correlations varying between −0.19 and 0.51, the median of 0.13 and similar global pattern (Fig. 5c). The latter suggests that when the mid-troposphere jet increase in intensity, it is conjoined with the higher vapour content, i.e., when the atmospheric conditions become more unstable on the vertical, more favourable conditions are present for the generation of NSLOTTs (Tanaka, 2010). Correlations with the low-troposphere vertical temperature gradient (with 50 hPa difference) are quasi-equally occurring as positive and negative at the sites (Fig. 5d), varying between −0.35 and 0.4 with the median of −0.05 (Fig. 4). Positive correlation signifies that, during the increase of the NSLOTT range, upper layers of the lower troposphere are heated while lower layers are cooled, which may indicate existence of a temperature inversion, found during the

Mediterranean meteotsunamis (e.g., Vilibić and Šepić, 2009; Jansà and Ramis, 2021). Interestingly, correlations are dominantly positive over the east oceans' coastlines and negative over the west coastlines, suggesting different vertical temperature conditions connected to NSLOTTs. More precisely, on the US West Coast, correlations are mainly negative, with the exception of Alaska having slightly positive values, while positive correlations dominate over the US East Coast. Negative correlations are also found over the coast of Chile, New Zealand and over the entire Western Mediterranean and Western and Northern Europe, while positive correlations prevail in the Eastern Mediterranean, Baltic Sea and over the eastern coast of Japan.

The second analysis is based on the horizontal correlations of NSLOTTs with the synoptic conditions. The correlation between the NSLOTT range and 550-hPa level geopotential horizontal differences (gradients) indicates the presence of an intense gradients at mid-troposphere levels during pronounced NSLOTT events (Fig. 6). Fig. 6b shows that the strongest correlations are placed on the southeast-northwest line relatively to the position of the gauge. Following the geostrophic balance, NSLOTTs are presumably associated with the southwestern flow on the Northern Hemisphere and with the western to north-western flow on the Southern Hemisphere. As for the mid-troposphere winds, the correlations are strongest in the mid-latitudes, while much lower in tropical and subtropical belts. However, the correlations are generally lower than with mid-troposphere winds with values between −0.59 and 0.59 and the median of −0.22 (Fig. 4). Negative correlations along the US East Coast are clustered eastward of the reference gauge, while Mediterranean gauges form a cluster towards southeast (not shown). This implies that NSLOTTs occurring in both areas are connected to the higher geopotential systems spreading to the east or southeast. The group of the points around the reference gauge on Fig. 6b corresponds to the stations at the US West Coast, suggesting that NSLOTTs in this region are adjoined to the systems located close to the affected area. Some maximum correlations are reached for grid points
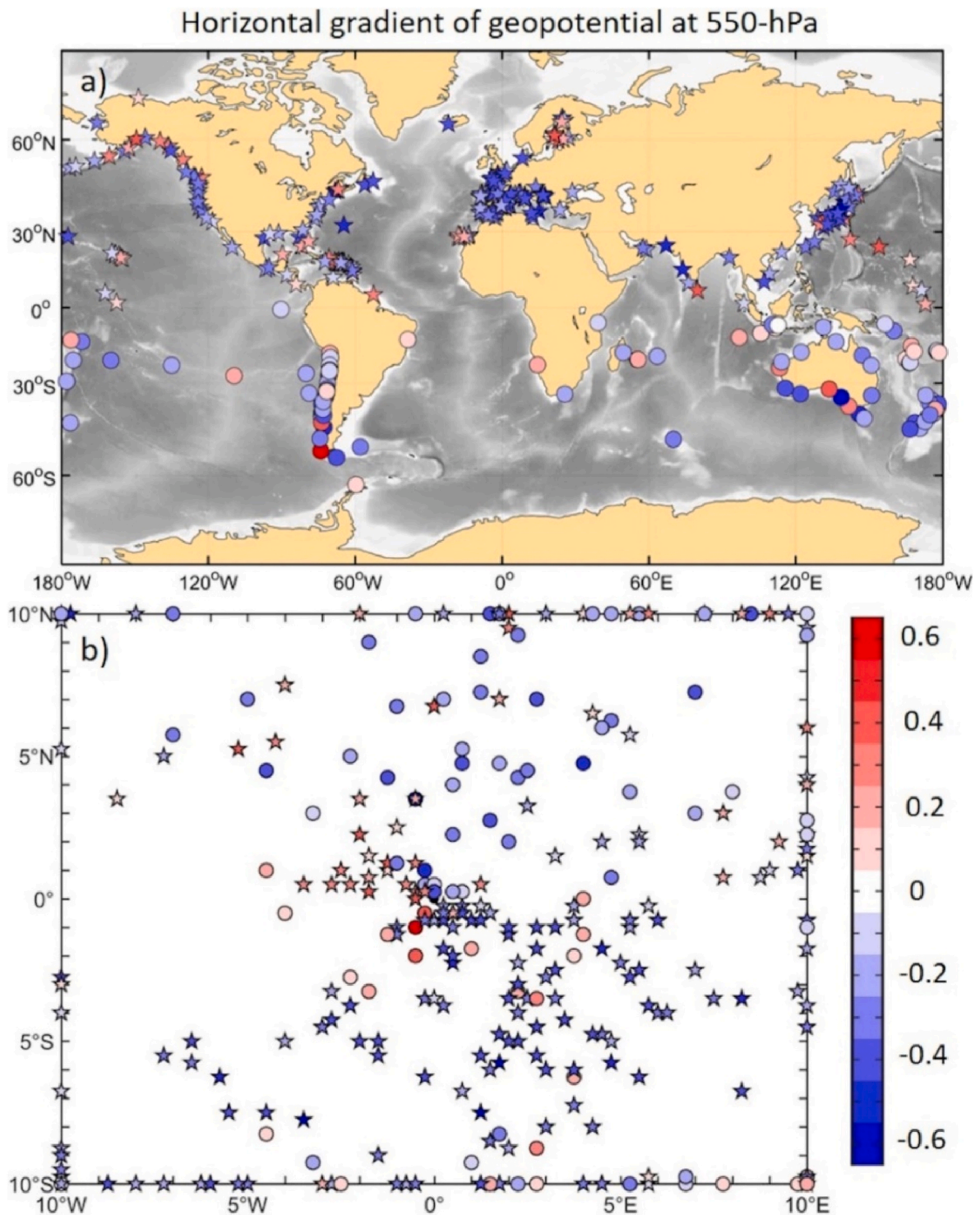
Horizontal gradient of geopotential at 550-hPa

Fig. 6. a) World map of maximum correlation coefficient between the NSLOTT range and horizontal gradient of geopotential at 550-hPa level between ERA5 grid point closest to a tide gauge and any point in a rectangle [-10°, 10°] latitude and [-10°, 10°] longitude around the station, and b) the position of the point relative to the point closest to a tide gauge for each station for which maximum correlation (shown by colour) has been achieved. Stars denote stations on the Northern Hemisphere, while circles denote stations on the Southern Hemisphere. (For interpretation of the references to colour in this figure legend, the reader is referred to the Web version of this article.)

along the boundary of the rectangle, pointing that they might reach higher values if a bigger rectangle is chosen for an ERA5 variable.

The next variable is mean sea-level pressure gradient, where opposite signs of the correlations indicate whether the maximal correlation to a tide gauge grid point is reached towards or off the cyclone (Fig. 7). The correlations span between −0.67 and 0.71 with the median of −0.23

(Fig. 4). On the Northern Hemisphere a cyclone is largely spreading north to northwest of a tide gauge, which is in agreement with the regional study of the high-frequency sea-level oscillations in the Mediterranean Sea (Šepić et al., 2015a). For the Japanese stations, highest correlations are obtained on the left edge of the observed rectangle (10° W of the reference tide gauge), unlike Chilean stations that have highest
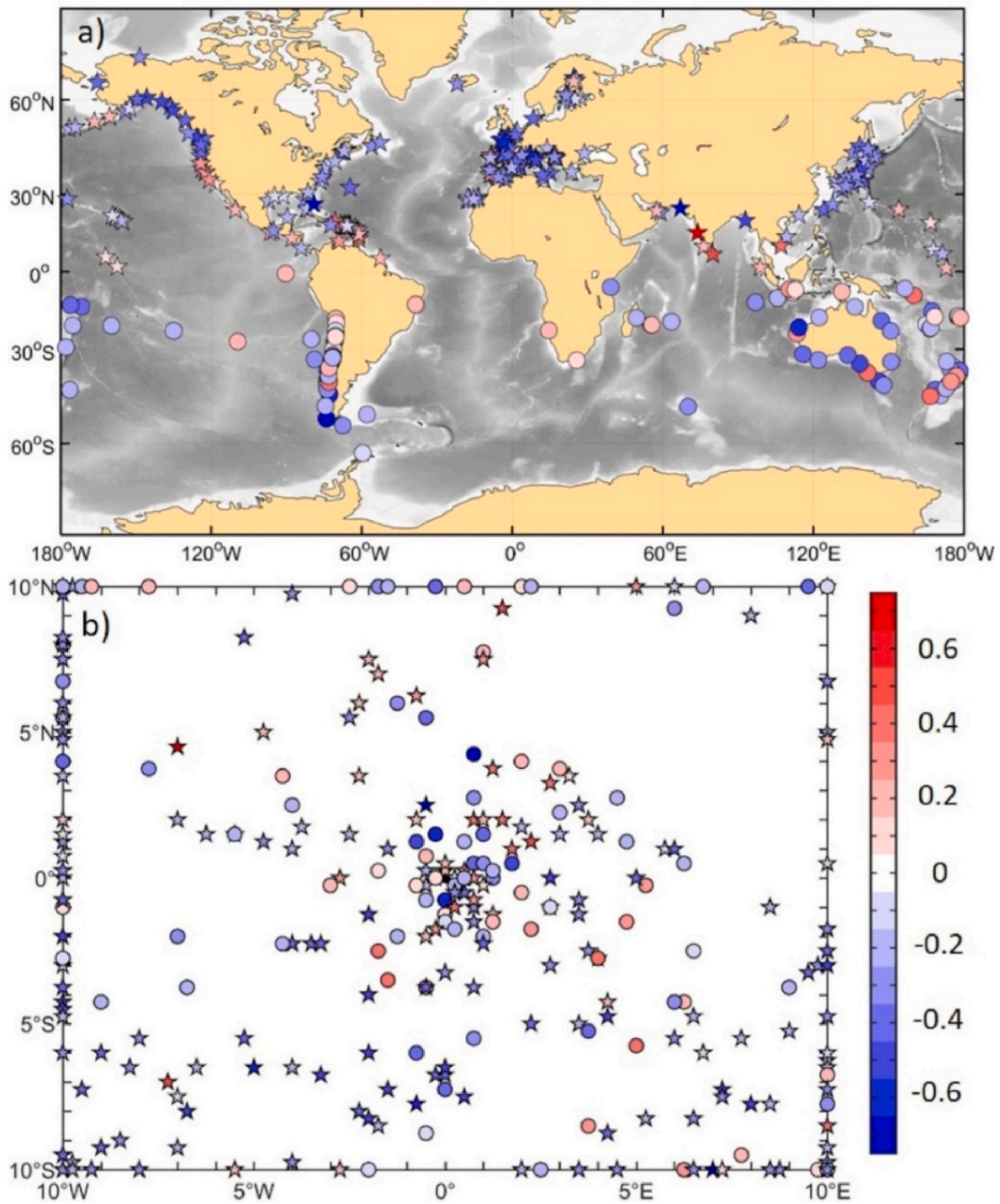
Fig. 7. As in Fig. 5, but for horizontal gradient of mean sea-level pressure.

correlations grouped close to the reference gauge, suggesting that NSLOTTs occurring in Japan are shaped by a thousand-km-far synoptic systems towards west, while being determined with systems positioned much closer to the affected stations in Chile. Stations on the US West Coast obtain highest correlations off the cyclone, as being shifted towards southeast.

The correlations are somewhat weaker with the 850-hPa level temperature gradient, between −0.57 and 0.50 with the median of 0.06 (Fig. 4). The strongest correlations are reached when the colder air is placed northwest and warmer air southeast of the station on the Northern Hemisphere, while the ordinarily opposite situation is seen on the Southern Hemisphere, with warmer air northeast and colder air southwest of the station (Fig. 8). NSLOTTs occurring at the US East Coast are mostly connected to the lower temperature systems shifted towards the west-northwest. In the Mediterranean Sea the situation is twofold – NSLOTTs in the Eastern and Western Mediterranean are mostly adjoined to higher temperature systems spreading southeast of the gauges with recorded oscillations, yet in the Central Mediterranean strongest connection is achieved with lower temperature systems to the northwest.

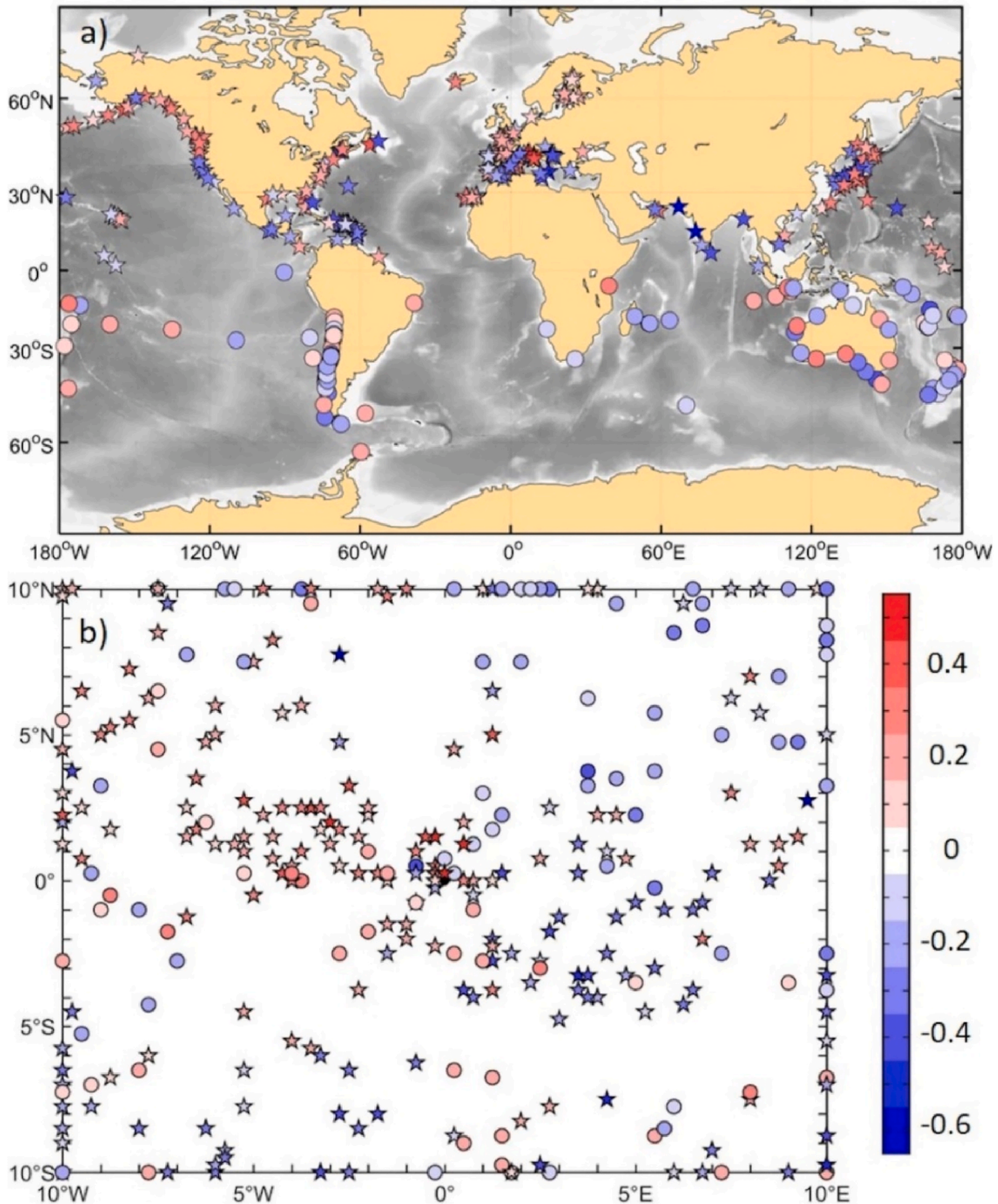## Horizontal gradient of temperature at 850-hPa level

Fig. 8. As in Fig. 5, but for horizontal gradient of temperature at 850-hPa level.

4. Atmosphere setup during meteotsunami events

In this section common synoptic patterns during extreme meteotsunami events are investigated. First, the Mediterranean Sea is chosen as the test case, as many synoptic variables are strongly correlated with NSLOTTs in this region. Fig. 9 shows the synoptic patterns of wind speed at 550 hPa, mean sea-level pressure and temperature at 850 hPa averaged over 10 extreme NSLOTT events (i.e., meteotsunamis) for 4 rectangle areas stretching 10° in latitude and longitude around the stations

located in (i) Almeria, Spain, (ii) Formentera, Spain, (iii) Vela Luka, Croatia, and (iv) Peiraias, Greece. During the meteotsunami events recorded on the tide gauge station in Almeria, strong south-westerly winds at 550 hPa level reach in average their maximum speed of 28 m/s over the Strait of Gibraltar. Along with the mid-troposphere jet stream, a weak low-pressure system with a minimum over the central Iberian Peninsula stretches over the whole considered area, except for the Atlantic coast of Spain and Northern Africa. Consequently, an inflow of warm air in the low troposphere (850 hPa level) is present over the
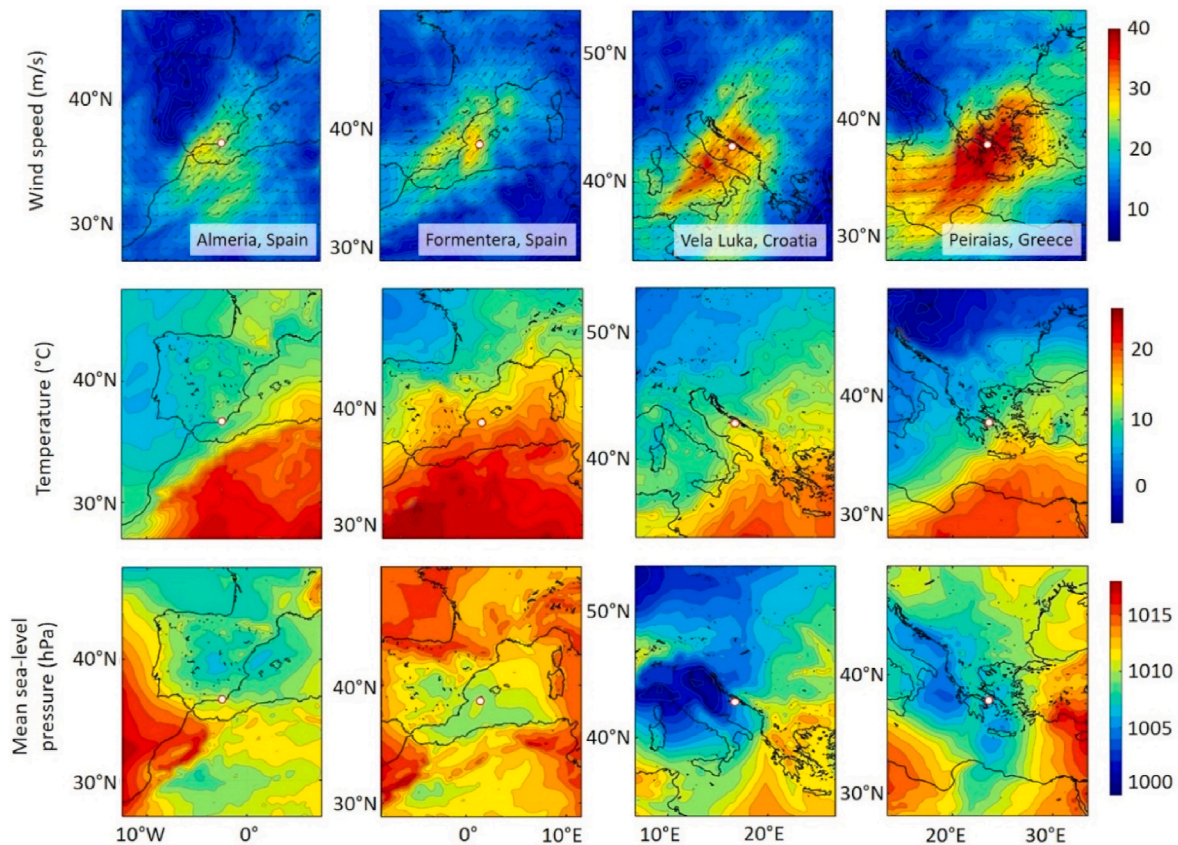
Fig. 9. Wind speed and direction at 550-hPa level, temperature at 850-hPa level and mean sea-level pressure averaged over all extreme NSLOTT events for 4 selected stations in the Mediterranean Sea.

whole western North Africa with temperatures surpassing 21 °C and the thermal front stretching in the southwest-northeast direction over the whole western North Africa coastal region.

Interestingly, the patterns linked to meteotsunami events in Formentera, Spain are similar to those connected to the events in Almeria. A weak cyclone of similar intensity and size than the Almeria one, is centred around the station and the mid-troposphere jet is parallel to the Mediterranean coast of Spain with its maximum positioned right next to the station, to the west. Winds are blowing towards the northeast with a speed reaching up to 29 m/s. The thermal front at 850 hPa lays over the central Spain and further followed the coast of France, with higher latitudinal inclination than during the events in Almeria.

The patterns during meteotsunami events in the third considered area, around Vela Luka, Croatia are characterized by a much deeper cyclone located over the Northern Italy. The Vela Luka station is positioned at the south-eastern perimeter of the low-pressure system. The mid-troposphere jet has much stronger south-westerly winds than at Almeria and Formentera, with speed up to 36 m/s crossing the Italian Peninsula, all the way from the Tunisia to the central Balkans. The thermal front at 850 hPa with SW-NE orientation is placed in parallel and at the south-eastern section of the mid-troposphere jet.

Further to the east, at Peiraias, Greece, the meteotsunami events are accompanied by quite strong mid-troposphere winds with speed reaching nearly 40 m/s. However, all other common characteristics (i.e., minimum in mean sea-level pressure centred or to the northwest of the tide gauge site and SW-NE oriented thermal front at 850-hPa level at the south-eastern perimeter of the mid-troposphere jet) are kept.

The analysis in the Mediterranean Sea shows that meteotsunami events are associated with different mid-troposphere jet speeds. This can be explained by the fact that atmosphere-ocean resonant conditions (the main generation mechanism of meteotsunami events) occur at different

depths in front of the tide gauge stations and are thus characterized by different tsunami wave speeds known to be equal to mid-troposphere jet speeds in wave-ducting conditions (Lindzen and Tung, 1976; Monserrat and Thorpe, 1996). Despite these differences, synoptic patterns during meteotsunami events are found to have strong similarities over the Mediterranean Sea, differing only in the intensity and precise location of the patterns including the mid-troposphere jet and the surface cyclones. This is in good agreement with the previous findings of the regional meteotsunami studies in the Mediterranean Sea (e.g., Šepić et al., 2009; Šepić et al., 2015a).

However, the main question raised by the previous regional analysis is: can common synoptic patterns be found at the global scale during meteotsunami events? To answer, Fig. 10 provides, separately for the Northern and Southern Hemisphere, the atmospheric fields averaged during meteotsunami events for stations which have correlation higher than 0.4 between the hourly NSLOTT range and the mid-troposphere wind speed. This wind is recognized as a crucial factor for NSLOTT generation and presumably reflects wave-ducting as the dominant process for the propagation of the meteotsunamigenic disturbances (e.g. Tanaka, 2010, Šepić et al., 2015a; 2015b; Vilibić and Šepić, 2017). It is found that only around 20% of all stations satisfy this condition: 27.1% from the stations located on the Northern Hemisphere and 11.3% from stations located on the Southern Hemisphere. Fig. 10 reveals that strong mid-troposphere jet streams inclined toward poles are present during meteotsunami events on both hemispheres, stretching from WSW to ENE on the Northern Hemisphere and from NW to SE on the Southern Hemisphere. The average wind speed, for all stations and all meteotsunami events, reaches 32 m/s at both hemispheres, with the maximum being shifted to the west of the reference station. On the Northern Hemisphere winds are in average not strongly inclined toward the North Pole, blowing from west-southwest, while being more inclined towards
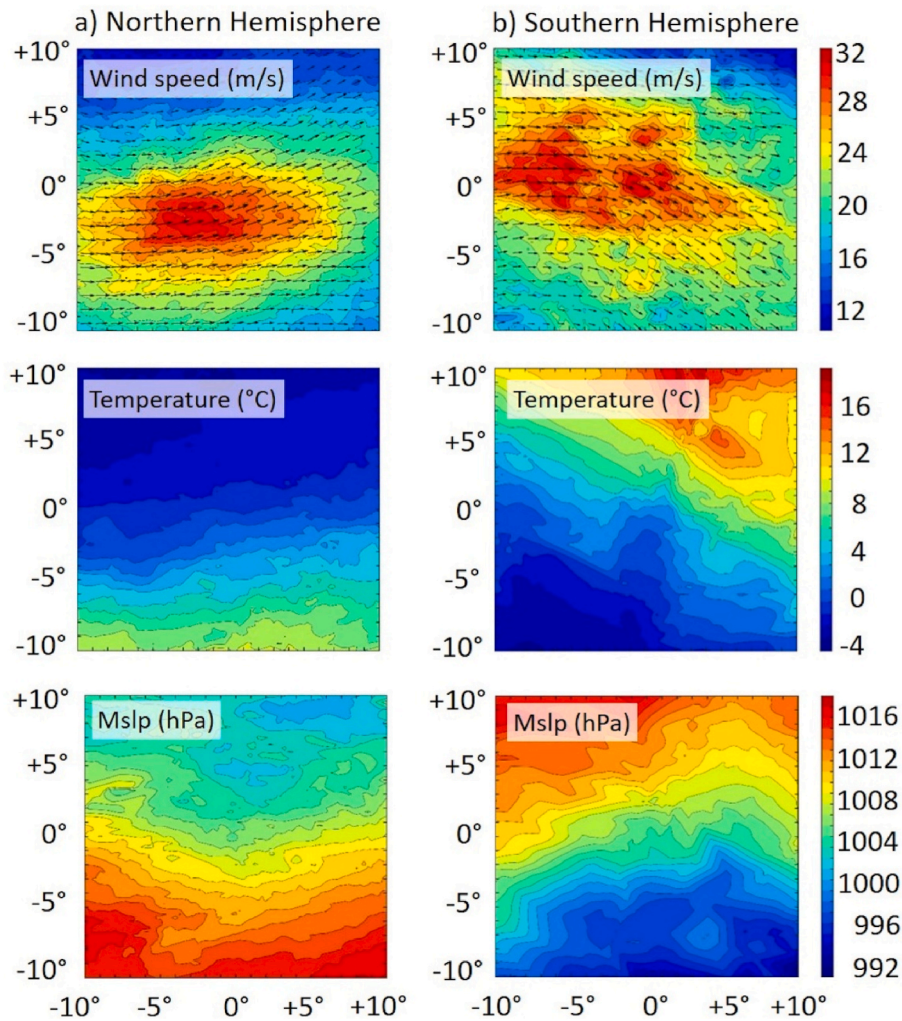
Fig. 10. Wind speed and direction at 550-hPa level, temperature at 850-hPa level and mean sea-level pressure averaged over all extreme NSLOTT events for the stations which have correlation between wind speed and NSLOTT range higher than 0.4 on the a) Northern, and b) Southern Hemisphere.

the South Pole on the Southern Hemisphere, blowing from northwest. On both hemispheres, low-pressure systems are centred poleward from the tide gauge sites. Finally, the thermal front in the lower troposphere is placed below the mid-troposphere jet on both hemispheres, but is much stronger on the Southern Hemisphere. Further, the Southern Hemisphere thermal front is embedding a wave-like disturbance crossing the tide gauge station. Such a difference is probably related to the intensity of low-pressure systems and the associated cold fronts, that are much deeper and stronger in the Southern Hemisphere during meteotsunami events.

5. NSLOTT index

In this last section, the global NSLOTT index is presented and analysed, estimated using the whole sea-level dataset at a station. First, Fig. 11 shows the first and second synoptic variables chosen for the construction of the global NSLOTT index μ. Mid-troposphere wind speed is the most commonly selected first variable (for about a third of all stations), as having the highest correlation with NSLOTTs of all synoptic variables. It is especially dominant in the northern West Coast of the US, the whole Mediterranean and Baltic regions and the southern coasts of Japan, Australia and Chile. These are all mid-latitude locations where its correlation with NSLOTTs are generally higher. The next most common synoptic variable selected as the first variable for μ is the horizontal gradient in mean sea-level pressure, which illustrates surface low-

pressure system in the vicinity of the affected station. This variable is often chosen in mid-latitudes and equatorial regions and reach 28% of all stations in total.

Interestingly, some stations located in the Northern Europe, northern coast of Japan, across the Chilean coast, but mainly along the West coast of the US have only one synoptic variable included in the NSLOTT index (Fig. 11b), as adding any second synoptic variable does not increase correlations more than 0.01. In fact, about 32% of stations do not have the second variable included in the index (Table 2). The variable that is chosen most often as the second variable of the index at the remaining stations is the relative humidity in the mid-troposphere (Fig. 11b). Moreover, around 57% of the stations that have mid-troposphere wind speed as the first chosen variable, have mid-troposphere relative humidity as the second variable in the NSLOTT index. Convincingly, the mid-troposphere jet with embedded instabilities is associated with NSLOTTs at a large number of stations, indicating that wave-ducting in the lower troposphere, which reflects the energy towards the surface, is a mechanism that is in favour of the longevity of intense atmospheric disturbances and the associated meteotsunami events.

Table 2 also emphasizes the importance of the mid-troposphere wind speed, as it is included in the NSLOTT index at more than half of the stations. The wind is then followed by mean sea-level pressure gradient and surface wind speed. Further, the index includes relative humidity above tide gauge and geopotential horizontal gradient in mid-troposphere, as well as low-level temperature horizontal gradient, all
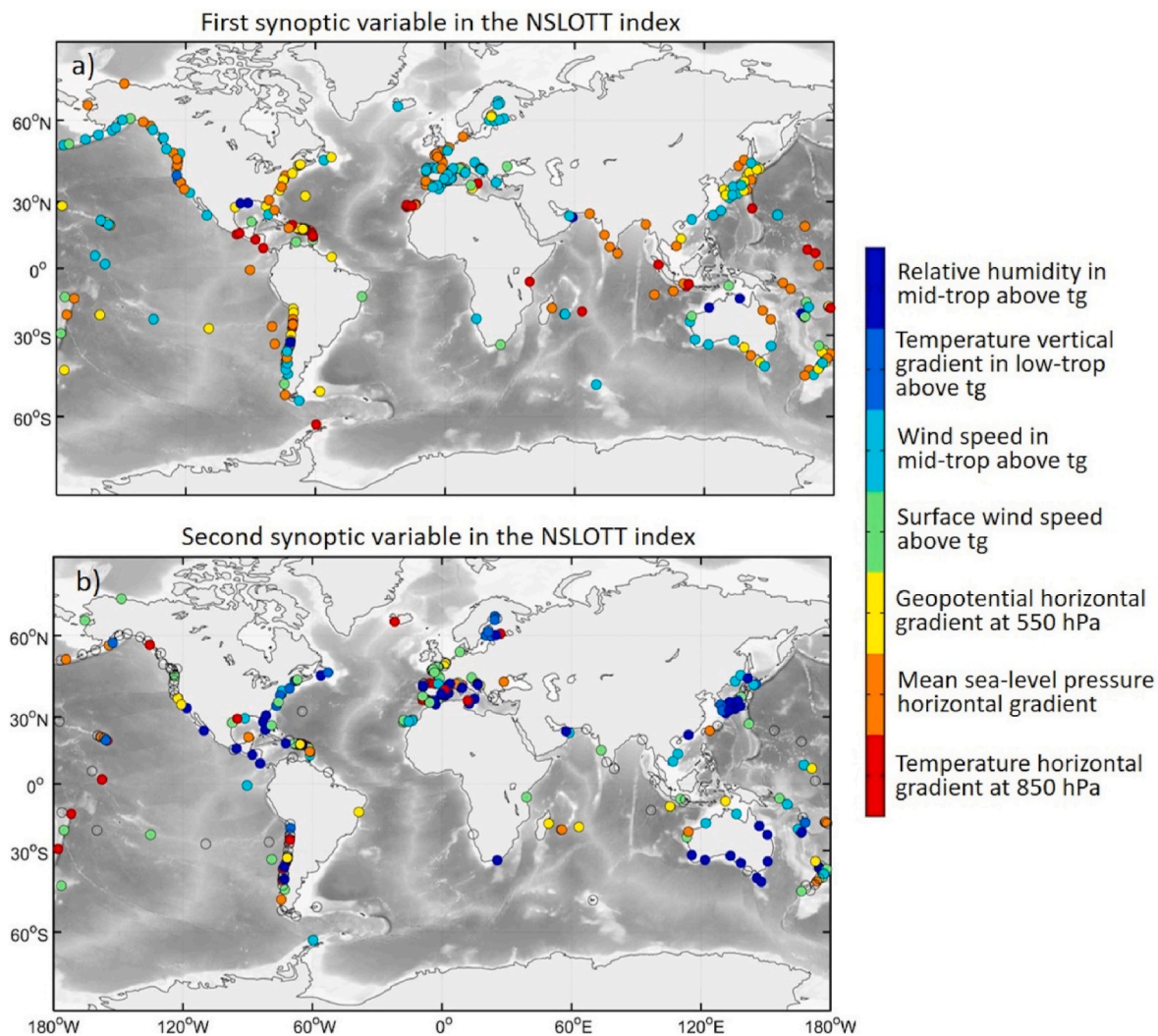
Fig. 11. World map of a) the first, and b) the second synoptic variable chosen for construction of the NSLOTT index at each station.

Table 2
Percentage of the synoptic variables used in the NSLOTT index.

Synoptic variables	% of use in μ
Wind speed in mid-troposphere above tide gauge	53.75%
Mean sea-level pressure horizontal gradient	42.02%
Surface wind speed	32.25%
Relative humidity in mid-troposphere above tide gauge	30.94%
Geopotential horizontal gradient at 550 hPa	30.29%
Temperature horizontal gradient at 850 hPa	27.69%
Temperature vertical gradient in low-troposphere above tide gauge	12.05%

Table 3
Percentage of the type of index (μ_1 - μ_7) used as the NSLOTT index.

μ_n	% of μ_n in μ
μ_1	31.60%
μ_2	25.73%
μ_3	27.69%
μ_4	12.70%
μ_5	1.63%
μ_6	0.65%
μ_7	0%

used at approximately same number of stations. Finally, temperature vertical gradient on low levels is the least used variable in the NSLOTT index, at only 12% of stations.

Among seven synoptic variables, only one is used in the construction of the NSLOTT index at nearly third of all stations (Table 3). Two variables are included in the NSLOTT index at around quarter of stations, while three variables constitute the index at somewhat over the quarter of stations. Further, four variables compose the index at 39 stations, while only 5 and 2 stations have the NSLOTT index with five and six variables, respectively. Indicatively, none of the stations have the index that include all seven considered synoptic variables.

Fig. 12 shows the time series of normalized values of the NSLOTT range and NSLOTT index for the period of 6 months at 4 different tide gauge stations located in the Cordova (US West Coast), Saint Pierre et Miquelon (northwest Atlantic Ocean), Port Ferréol (Mediterranean coast of France) and Tosashimizu (southern coast of Japan). The NSLOTT index and range time-series roughly follow the same patterns at all considered stations, yet at some stations the agreement between the series is higher depending on the obtained correlations. For example, at the station Port Ferréol, which has one of the highest correlations (0.76), the curves of the NSLOTT index and the NSLOTT range have quite a satisfactory matching during the considered period, however the local maxima of sea-level series are not adequately followed by the index values. This is even more pronounced at other stations, especially at Saint Pierre et Miquelon and Tosashimizu where a moderate correlation is obtained for the whole period of stations' activity (0.51, 0.46).
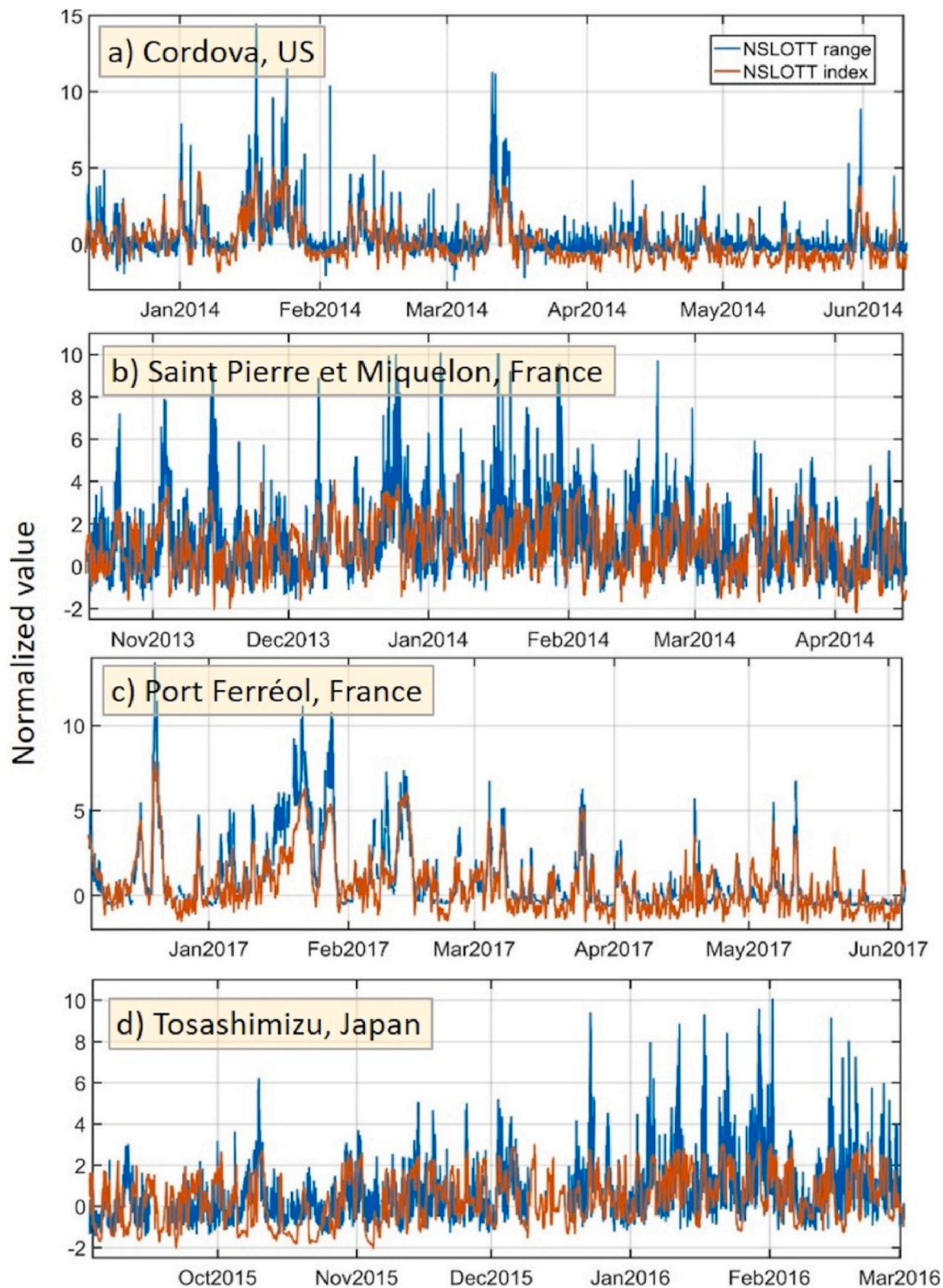
Fig. 12. Time series of the normalized NSLOTT range and normalized NSLOTT index during 1 month at stations a) Cordova, US, b) Saint Pierre et Miquelon, France, northwest Atlantic Ocean, c) Port Ferréol, France, and d) Tosashimizu, Japan.

The correlation between the NSLOTT index and the NSLOTT range is shown in Fig. 13. The highest values of correlation, mostly surpassing 0.5 and reaching up to 0.8, are found in the Mediterranean region. While the US West Coast and the Japanese coastline are almost homogenous,

with correlations between 0.3 and 0.5, more variability in correlation is found along the US East Coast, in Chile and in the Baltic Sea. The median value of the correlation is 0.38 for all the stations included, but correlation values are highly variable from region to region and even from
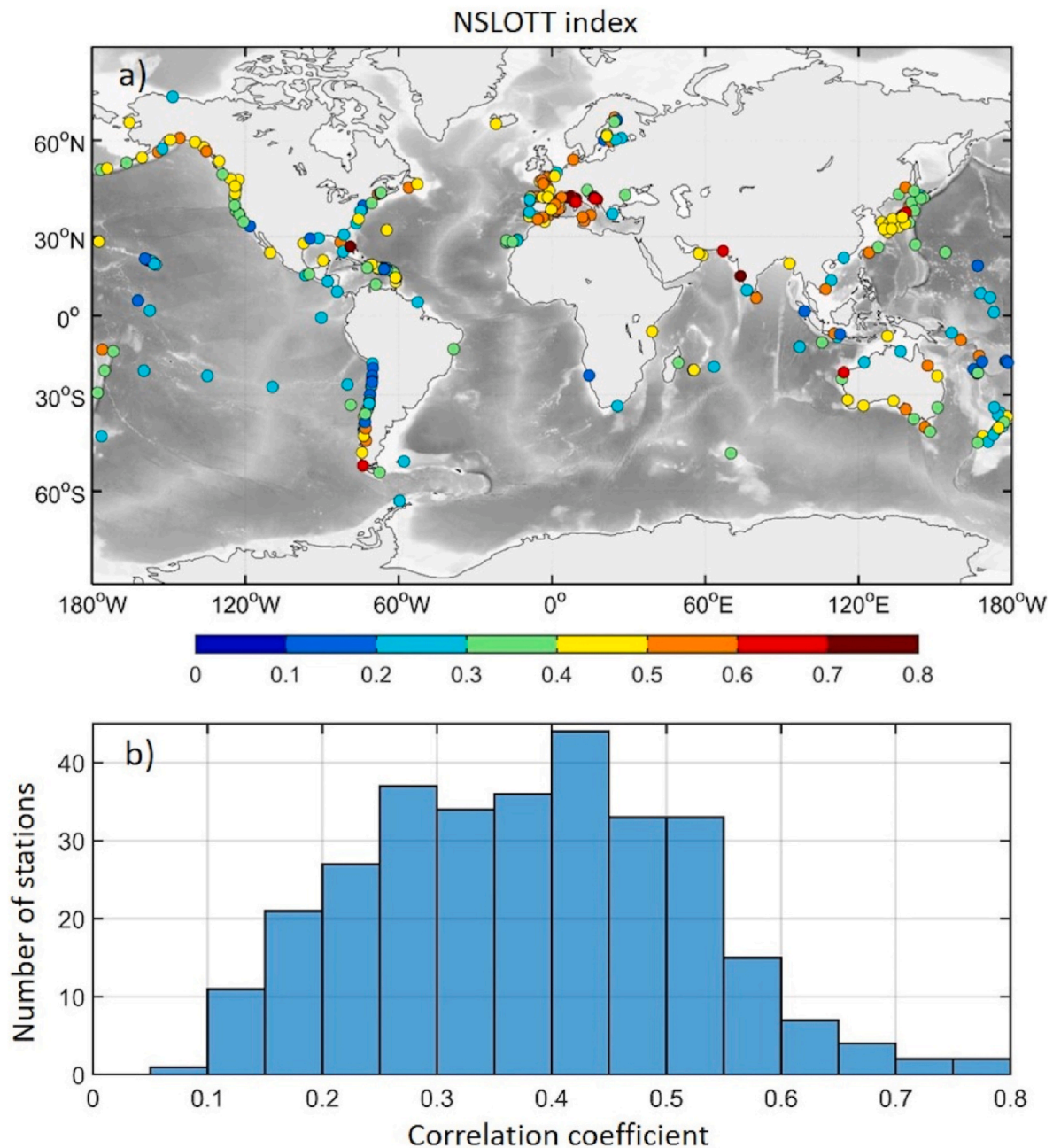
Fig. 13. a) World map of correlation coefficient between the NSLOTT range and NSLOTT index, and b) distribution of the correlation coefficient.

station to station, spanning in the interval between 0.09 and 0.76. This suggests that various intensities of connection between the defined index and NSLOTTs can be found worldwide.

The global NSLOTT index may thus not be optimal at each of the 307 stations considered in this study, but its systematic derivation enables to identify meteotsunami events from synoptic conditions at the global scale.

6. Discussion

The connection between meteotsunamis and NSLOTTs with specific synoptic conditions has been demonstrated in this study over the entire globe while previous studies only quantified them for the Balearic Islands (Šepić et al., 2016). It should be highlighted that our analyses are insensitive to local bathymetry (and therefore local wave amplification) characteristics around a tide gauge, which may influence regression

coefficients only but not correlations themselves when pairing high-frequency sea-level series (NSLOTT series) with synoptic variables and the NSLOTT index. When considering synoptic variables individually, correlations are rarely strong. However, particular combinations of variables are shown to coincide with NSLOTTs in some regions obtaining medium to strong correlations. The region with the highest correlations is found to be the Mediterranean Sea. These results are in line with the previous studies describing similar atmospheric setup during pronounced NSLOTT and meteotsunami events (Belušić and Strelec Mahović, 2009; Šepić et al., 2009, 2015a). Consequently, the presented methodology is deemed appropriate for global studies even though detailed local analyses should always be carried out at a site level as the difference between intensity of NSLOTTs may vary substantially in space (Zemunik et al., 2022). In contrast, the tropics have obtained generally lower correlations of NSLOTTs (which are anyhow of lower intensity there, Zemunik et al., 2022) with the synoptic variables and with the

estimated NSLOTT index, suggesting that described methodology is not very suitable for these regions.

It is important to notice that the choice of the synoptic variables used in this study mostly relied on the predetermined atmospheric patterns recognized during strong NSLOTT events in the Mediterranean Sea. This can be considered as a weakness of the methodology because patterns and variables in favour of NSLOTTs may strongly differ from region to region. For example, a common propagation mechanism of NSLOTTs and meteotsunamis in the Mediterranean is wave-ducting (Plougonven and Zhang, 2014) which is characterized by the propagation of atmospheric gravity waves below the mid-troposphere jet streams which generate instabilities. However, the jet may change in height between different regions, so the choice of this height may be important in representing this specific synoptic variable. To this aim, correlations of NSLOTTs with wind speed (and other vertical variables) at different pressure levels (from 700 to 400 hPa) were tested. It was found that changes in height are insignificant concerning the correlations between NSLOTT and synoptic conditions as the wave-duct mechanism is shaping the vertical wind profile at all heights between the surface and the mid-troposphere (Lindzen and Tung, 1976; Monserrat and Thorpe, 1996). However, other mechanisms, such as wave-CISK (Convective Instability of the Second Kind, Powers and Reed, 1993), frontal passages or squall lines are found to be associated with NSLOTTs in some other regions in the world (e.g., Great Lakes, Bechle et al., 2016; Chilean coast, Vilibić and Šepić, 2017; Northwest Europe, Williams et al., 2021). Further, the atmospheric processes generating the meteotsunamigenic disturbances remain to be studied in detail in particular concerning the role of orography and convection (Plougonven and Zhang, 2014). For orography, no study quantified its role during meteotsunamis, aside from Denamiel et al. (2022) which show that no significant change in meteotsunami intensity is reproduced in the Adriatic in simulations with and without orography. For convection, it can result from tropical cyclones and hurricanes, for example, whose peripheral rain bands may generate meteotsunamis (Shi et al., 2020). Tropical cyclones are, however, characterized by quite opposite synoptic patterns than the one described during mid-latitude NSLOTTs – e.g., weak vertical shear and no jet stream (Frank and Ritchie, 1999; Emanuel et al., 2004). Therefore, the proposed NSLOTT methodology might be inappropriate in some regions, like our analysis indicated that it is in the tropics.

Another way to improve construction of the NSLOTT index from synoptic patterns, which is here potentially oversimplified by the linear combination of synoptic variables with weighting coefficients estimated using the least square method, is to use advanced clustering methods, such as Bayesian inference (Cheng et al., 2014) and machine learning algorithms (Leuenberger and Kanevski, 2015). The latter for extreme NSLOTT events may include neural networks (Cannon, 2012), Self-Organising Maps (Cassano et al., 2016) and deep learning (Yu and Ma, 2021) algorithms, which are proven to have capacity to learn on extremes in geosciences.

After quantifying connectivity between synoptic patterns and NSLOTTs or meteotsunamis, the established relations may be used for several applications. One is for warning systems of extreme NSLOTTs that could be built to provide forecasts a week in advance when atmospheric synoptic forecasts hold a reliability (Zhou et al., 2019). In fact, such a methodology is the basis for forecasting the Balearic rissagas (local meteotsunamis) regularly issued by the Spanish State Meteorological Agency since mid-1980 and based on qualitative assessment of the synoptic conditions by a forecaster (Jansà and Ramis, 2021). A more objective method was introduced by Vich and Romero (2021), who use neural networks to forecast rissaga amplitude through observed or forecasted atmospheric data. However, following the results of this study, such forecasts could be extended to a great portion of the global oceans, in particular at mid-latitudes, and their objectivity and automatization could be increased as based on quantifiable relations. Such forecasts could be produced by setting the criteria of index based on a certain period of time (a decade or so) and examining how well it predicts during the following years. This approach might improve rapid hazard and risk management in coastal regions prone to rapid sea level changes associated with strong currents which affect port operations (Pattiaratchi and Wijeratne, 2014), safety of navigation (Goring, 2009), coastal infrastructure (Huang et al., 2022), tourism (Šepić et al., 2018; Linares et al., 2019), safety of aquaculture farms (Vilibić et al., 2004), and other. However, this study is a global study of connectivity between synoptic patterns and NSLOTTs and for operational usage the targeted research should follow in the future. In addition, a coastal meteotsunami hazard upon which a warning is built is a function of many variables, including the threshold for coastal flooding (e.g., Denamiel et al., 2019a, 2019b). This variable is site-dependant and, to properly set up such a system, local parameters must be considered.

Another application could be to quantify NSLOTT climates at global scales, which are still based on short-term (up to a decade) sea-level measurements at a minute timescale (e.g., Dusek et al., 2019; Kim et al., 2021; Williams et al., 2021). Through such an approach, Šepić et al. (2016) provided a robust estimate of interannual variability and seasonal changes of meteotsunamis in the Balearic Islands. Here, it could be applied globally and regionally for basins where the NSLOTT index is strongly correlated to NSLOTT ranges, allowing for hazard assessments at the global scale. These estimates may be added to overall hazard estimates of sea level extremes, as NSLOTTs extremes may contribute to up to 50% of the sea level extremes in low-tidal basins, such as the Mediterranean (Šepić et al., 2015a). In this era of climate change, the next step might be to quantify the NSLOTT changes in future climates, following the estimates and the methodology already applied for the Balearic Islands (Vilibić et al., 2018). The latter study revealed that, in some climate scenarios, meteotsunami intensity may increase substantially (for about 30% till 2 100 in the RCP 8.5 greenhouse gas emission scenario). With all of this taken into a planning, the last component of the sea level budget, still not taken in coastal hazard assessment studies (Stephens et al., 2021), may be finally used in coastal planning and risk estimates at high resolution.

7. Summary and conclusions

Short-period sea-level oscillations, their characteristics, generation mechanisms, and impacts are still under-investigated in all worlds' regions. The strongest NSLOTTs and meteotsunamis appear as recurrent flooding events in specific coastal locations, therefore they have been researched through location-oriented or regional studies at most. To overcome such an approach, Zemunik et al. (2022) quantified globally different aspects of NSLOTTs, while this study represents the very first attempt to quantify global connections between NSLOTTs and synoptic patterns. The patterns are represented by variables which are documented locally to conjoin meteotsunamis. The following major conclusions can be derived:

1. Mid-troposphere wind speed is the synoptic variable having highest correlations with the NSLOTT ranges and being included in the NSLOTT index estimates at more than half of the stations. As the extreme NSLOTT and meteotsunamis are generated by travelling atmospheric disturbances, this points to their generation largely occurring within the mid-troposphere jet. Further, the atmospheric disturbances are presumably generated at the front sections of mid-troposphere jets, as the core of the jet is normally located west from the tide gauge where extreme NSLOTTs are documented.

2. At stations where the mid-troposphere wind speed has the highest correlations with NSLOTTs, the mid-troposphere relative humidity has the second highest correlations, resembling instabilities present in the mid-troposphere jet and presuming dominance of the wave-ducting mechanism that keeps the energy towards the sea surface during for the NSLOTT generation.

3. Temperature vertical gradient in lower troposphere has weakest correlations with the NSLOTT ranges and is the least used variable in

the NSLOTT index. This implies that near-surface temperature inversion is not regularly conjoined with the extreme NSLOTT events.

4. Extreme NSLOTT events are accompanied with a specific synoptic pattern, including strong mid-troposphere jet streams with average speed up to 32 m/s, low-troposphere thermal front and surface cyclones in the vicinity of the affected area, with some differences spotted between hemispheres, as more pronounced thermal front and deeper cyclones are found on the Southern Hemisphere.

5. The NSLOTT index, constructed by using synoptic variables, obtained highest correlations with the NSLOTT ranges in the mid-latitudes, particularly in the Mediterranean Sea where it reaches 0.79, suggesting that the proposed methodology is most suitable for these areas.

6. For sites with high correlations, the NSLOTT index follows the variability of the NSLOTT ranges, i.e., times of local extrema are mostly conjoined in their time series. However, maximum ranges of NSLOTTs tends to be underestimated, particularly at the stations for which correlation is not high.

Author contributions

I. Vilibić and P. Zemunik developed the concept for the paper. P. Zemunik performed the analyses considering the comments and ideas raised by all authors, while C. Denamiel and J. Williams helped with coding and visualisation. P. Zemunik and I. Vilibić wrote the initial draft of the manuscript while all authors commented and revised the text.

Declaration of competing interest

The authors declare that they have no known competing financial interests or personal relationships that could have appeared to influence the work reported in this paper.

Acknowledgments

References

Bechle, A.J., Wu, C.H., Kristovich, D.A.R., Anderson, E.J., Schwab, D.J., Rabinovich, A. B., 2016. Meteotsunamis in the Laurentian Great Lakes. Sci. Rep. 6, 37832 https:// doi.org/10.1038/srep37832.

Belušić, D., Strelec Mahović, N., 2009. Detecting and following atmospheric disturbances with a potential to generate meteotsunamis in the Adriatic. Phys. Chem. Earth 34, 918–927. https://doi.org/10.1016/j.pce.2009.08.009.

Cannon, A.J., 2012. Neural networks for probabilistic environmental prediction: conditional density estimation network creation and evaluation (CaDENCE) in R. Comput. Geosci. 41, 126–135. https://doi.org/10.1016/j.cageo.2011.08.023.

Cassano, J.J., Cassano, E.N., Seefeldt, M.W., Gutowski, W.J., Glisan, J.M., 2016. Synoptic conditions during wintertime temperature extremes in Alaska. J. Geophys. Res. Atmos. 121 (7), 3241–3262. https://doi.org/10.1002/2015jd024404.

Cheng, L., AghaKouchak, A., Gilleland, E., Katz, R.W., 2014. Non-stationary extreme value analysis in a changing climate. Climatic Change 127, 353–369. https://doi. org/10.1007/s10584-014-1254-5.

Cook, R.D., Su, Z., Yang, Y., 2015. envlp: a MATLAB toolbox for computing envelope estimators in multivariate analysis. J. Stat. Software 62 (8), 1–20. https://doi.org/ 10.18637/jss.v062.i08.

Denamiel, C., Šepić, J., Ivanković, D., Vilibić, I., 2019a. The Adriatic Sea and Coast modelling suite: evaluation of the meteotsunami forecast component. Ocean Model. 135, 71–93. https://doi.org/10.1016/j.ocemod.2019.02.003.

Denamiel, C., Šepić, J., Huan, X., Bolzer, C., Vilibić, I., 2019b. Stochastic surrogate model for meteotsunami early warning system in the eastern Adriatic Sea. J. Geophys. Res. Oceans 124, 8485–8499. https://doi.org/10.1029/2019JC015574.

Denamiel, C., Tojčić, I., Vilibić, I., 2022. Meteotsunamis in orography-free, flat bathymetry and warming climate conditions. J. Geophys. Res. Oceans 127 (1). https://doi.org/10.1029/2021JC017386.

Dusek, G., DiVeglio, C., Licate, L., Heilman, L., Kirk, K., Paternostro, C., Miller, A., 2019. A meteotsunami climatology along the U.S. East Coast. Bull. Am. Meteorol. Soc. 100, 1329–1345. https://doi.org/10.1175/BAMS-D-18-0206.1.

Emanuel, K., DesAutels, C., Holloway, C., Korty, R., 2004. Environmental control of tropical cyclone intensity. J. Atmos. Sci. 61 (7), 834–858. https://doi.org/10.1175/ 1520-0469(2004)061<0843:ECOTCI>2.0.CO;2.

Frank, W.M., Ritchie, E.A., 1999. Effects of environmental flow upon tropical cyclone structure. Mon. Weather Rev. 127 (9), 2044–2061. https://doi.org/10.1175/1520-0493(1999)127<2044:EOEFUT>2.0.CO;2.

Goring, D.G., 2009. Meteotsunami resulting from the propagation of synoptic-scale weather systems. Phys. Chem. Earth 34 (17–18), 1009–1015. https://doi.org/ 10.1016/j.pce.2009.10.004.

Haigh, I.D., Marcos, M., Talke, S.A., Woodworth, P.L., Hunter, J.R., Hague, B.S., Arns, A., Bradshaw, E., Thompson, P., 2022. GESLA Version 3: a major update to the global higher-frequency sea-level dataset. Geosci. Data J. https://doi.org/10.1002/ gdj3.174.

Hersbach, H., Bell, B., Berrisford, P., Hirahara, S., Horányi, A., Muñoz-Sabater, J., Nicolas, J., Peubey, C., Radu, R., Schepers, D., Simmons, A., Soci, C., Abdalla, S., Abellan, X., Balsamo, G., Bechtold, P., Biavati, G., Bidlot, J., Bonavita, M., De Chiara, G., Dahlgren, P., Dee, D., Diamantakis, M., Dragani, R., Flemming, J., Forbes, R., Fuentes, M., Geer, A., Haimberger, L., Healy, S., Hogan, R.J., Hólm, E., Janisková, M., Keeley, S., Laloyaux, P., Lopez, P., Lupu, C., Radnoti, G., de Rosnay, P., Rozum, I., Vamborg, F., Villaume, S., Thépaut, J.-N., 2020. The ERA5 global reanalysis. Q. J. R. Meteorol. Soc. 146, 1999–2049. https://doi.org/10.1002/ qj.3803.

Holgate, S.J., Matthews, A., Woodworth, P.L., Rickards, L.J., Tamisiea, M.E., Bradshaw, E., Foden, P.R., Gordon, K.M., Jevrejeva, S., Pugh, J., 2013. New data systems and products at the permanent Service for mean sea level. J. Coast Res. 288, 493–504. https://doi.org/10.2112/jcoastres-d-12-00175.1.

Huang, C., Anderson, E., Liu, Y., Ma, G., Mann, G., Xue, P., 2022. Evaluating essential processes and forecast requirements for meteotsunami-induced coastal flooding. Nat. Hazards 110, 1693–1718. https://doi.org/10.1007/s11069-021-05007-x.

Jansà, A., Ramis, C., 2021. The Balearic rissaga: from pioneering research to present-day knowledge. Nat. Hazards 106, 1269–1297. https://doi.org/10.1007/s11069-020-04221-3.

Jansà, A., Monserrat, S., Gomis, D., 2007. The rissaga of 15 June 2006 in Ciutadella (Menorca), a meteorological tsunami. Adv. Geosci. 12, 1–4. https://doi.org/ 10.5194/adgeo-12-1-2007.

Kim, M.-S., Woo, S.-B., Eom, H., You, S.H., 2021. Occurrence of pressure-forced meteotsunami events in the eastern Yellow Sea during 2010-2019. Nat. Hazards Earth Syst. Sci. 21, 3323–3337. https://doi.org/10.5194/nhess-21-3323-2021.

Lee, S., 1999. Why are the climatological zonal winds easterly in the equatorial upper troposphere? J. Atmos. Sci. 56, 1353–1363. https://doi.org/10.1175/1520-0469 (1999)056<1353:WATCZW>2.0.CO;2.

Leuenberger, M., Kanevski, M., 2015. Extreme Learning Machines for spatial environmental data. Comput. Geosci. 85, 64–73. https://doi.org/10.1016/j. cageo.2015.06.020. Part B.

Linares, Á., Wu, C.H., Bechle, A.J., Anderson, E.J., Kristovich, D.A.R., 2019. Unexpected rip currents induced by a meteotsunami. Sci. Rep. 9, 2105. https://doi.org/10.1038/ s41598-019-38716-2.

Lindzen, R.S., Tung, K.-K., 1976. Banded convective activity and ducted gravity waves. Mon. Weather Rev. 104, 1602–1617. https://doi.org/10.1175/1520-0493(1976) 104<1602:BCAADG>2.0.CO;2.

Monserrat, S., Thorpe, A.J., 1996. Use of ducting theory in an observed case of gravity waves. J. Atmos. Sci. 53, 1724–1736. https://doi.org/10.1175/1520-0469(1996) 053<1724:UODTIA>2.0.CO;2.

Nomitsu, T., 1935. A theory of tsunamis and seiches produced by wind and barometric gradient. Memoirs Coll. Sci. Kyoto Imper. Univ. Ser. A 18 (4), 201–214.

Pattiaratchi, C., Wijeratne, E.M.S., 2014. Observations of meteorological tsunamis along the south-west Australian coast. Nat. Hazards 74 (1), 281–303. https://doi.org/ 10.1007/s11069-014-1263-8.

Plougonven, R., Zhang, F., 2014. Internal gravity waves from atmospheric jets and fronts. Rev. Geophys. 52, 33–76. https://doi.org/10.1002/2012RG000419.

Powers, J.G., Reed, R.J., 1993. Numerical simulation of the large amplitude mesoscale gravity-wave event of 15 December 1987 in the central United States. Mon. Weather Rev. 121, 2285–2308. https://doi.org/10.1175/1520-0493(1993)121<2285: NSOTLA>2.0.CO;2.

Rabinovich, A.B., Monserrat, S., 1996. Meteorological tsunamis near the Balearic and Kuril Islands: descriptive and statistical analysis. Nat. Hazards 13, 55–90. https:// doi.org/10.1007/bf00156506.

Rabinovich, A.B., Monserrat, S., 1998. Generation of meteorological tsunamis (large amplitude seiches) near the Balearic and Kuril Islands. Nat. Hazards 18, 27–55. https://doi.org/10.1023/A:1008096627047.

Rabinovich, A.B., Šepić, J., Thomson, R.E., 2021. The meteorological tsunami of 1 November 2010 in the southern Strait of Georgia: a case study. Nat. Hazards 106, 1503–1544. https://doi.org/10.1007/s11069-020-04203-5.

Ramis, C., Jansà, A., 1983. Condiciones meteorológicas simultáneas a la aparición de oscilaciones del nivel del mar de amplitud extraordinaria en el Mediterráneo Occidental. Rev. Geofisc. 39, 35–42.

Sibley, A., Cox, D., Long, D., Tappin, D., Horseburgh, K., 2016. Meteorologically generated tsunami-like waves in the North Sea on 1/2 July 2015 and 28 May 2008. Weather 71 (3), 68–74. https://doi.org/10.1002/wea.2696.

Stephens, S.A., Paulik, R., Reeve, G., Wadhwa, S., Popovich, B., Shand, T., Haughey, R., 2021. Future changes in built environment risk to coastal flooding, permanent inundation and coastal erosion hazards. J. Mar. Sci. Eng. 9, 1011. https://doi.org/10.3390/jmse9091011.

Šepić, J., Rabinovich, A.B., 2014. Meteotsunami in the great Lakes and on the Atlantic coast of the United States generated by the "derecho'' of June 29-30, 2012. Nat. Hazards 74, 75–107. https://doi.org/10.1007/s11069-014-1310-5.

Šepić, J., Vilibić, I., Monserrat, S., 2009. Teleconnections between the Adriatic and the Balearic meteotsunamis. Phys. Chem. Earth 34, 928–937. https://doi.org/10.1016/j.pce.2009.08.007.

Šepić, J., Vilibić, I., Strelec Mahović, N., 2012. Northern Adriatic meteorological tsunamis: observations, link to the atmosphere, and predictability. J. Geophys. Res. 117, C02002 https://doi.org/10.1029/2011JC007608.

Šepić, J., Vilibić, I., Lafon, A., Macheboeuf, L., Ivanović, Z., 2015a. High-frequency sea level oscillations in the Mediterranean and their connection to synoptic patterns. Prog. Oceanogr. 137, 284–298. https://doi.org/10.1016/j.pocean.2015.07.005.

Šepić, J., Vilibić, I., Rabinovich, A.B., Monserrat, S., 2015b. Widespread tsunami-like waves of 23-27 June in the Mediterranean and Black Seas generated by high-altitude atmospheric forcing. Sci. Rep. 5 (1), 11682 https://doi.org/10.1038/srep11682.

Šepić, J., Vilibić, I., Monserrat, S., 2016. Quantifying the probability of meteotsunami occurrence from synoptic atmospheric patterns. Geophys. Res. Lett. 43, 10377–10384. https://doi.org/10.1002/2016GL070754.

Šepić, J., Rabinovich, A.B., Sytov, V.N., 2018. Odessa tsunami of 27 June 2014: observations and numerical modelling. Pure Appl. Geophys. 175, 1545–1572. https://doi.org/10.1007/s00024-017-1729-1.

Shi, L.M., Olabarrieta, M., Nolan, D.S., Warner, J.C., 2020. Tropical cyclone rainbands can trigger meteotsunamis. Nat. Commun. 11, 678. https://doi.org/10.1038/s41467-020-14423-9.

Tanaka, K., 2010. Atmospheric pressure-wave bands around a cold front resulted in a meteotsunami in the East China Sea in February 2009. Nat. Hazards Earth Syst. Sci. 10 (12), 2599–2610. https://doi.org/10.5194/nhess-10-2599-2010.

Tappin, D.R., Sibley, A., Horsburgh, K., Daubord, C., Cox, D., Long, D., 2013. The English Channel "tsunami" of 27 June 2011 - a probable meteorological source. Weather 68 (6), 144–152. https://doi.org/10.1002/wea.2061.

Thomson, R.E., Rabinovich, A.B., Fine, I.V., Sinnott, D.C., McCarthy, A., Sutherland, N.A. S., Neil, L.K., 2009. Meteorological tsunamis on the coasts of British Columbia and Washington. Phys. Chem. Earth 34, 971–988. https://doi.org/10.1016/j.pce.2009.10.003.

Vich, M.-M., Romero, R., 2021. Forecasting meteotsunamis with neural networks: the case of Ciutadella harbour (Balearic Islands). Nat. Hazards 106, 1299–1314. https://doi.org/10.1007/s11069-020-04041-5.

Vilibić, I., Šepić, J., 2009. Destructive meteotsunamis along the eastern Adriatic coast: Overview. Phys. Chem. Earth 34, 904–917. https://doi.org/10.1016/j.pce.2009.08.004.

Vilibić, I., Šepić, J., 2017. Global mapping of nonseismic sea level oscillations at tsunami timescales. Sci. Rep. 7, 40818 https://doi.org/10.1038/srep40818.

Vilibić, I., Domijan, N., Orlić, M., Leder, N., Pasarić, M., 2004. Resonant coupling of a traveling air pressure disturbance with the east Adriatic coastal waters. J. Geophys. Res. 109 (C10) https://doi.org/10.1029/2004jc002279.

Vilibić, I., Šepić, J., Dunić, N., Sevault, F., Monserrat, S., Jordà, G., 2018. Proxy-based assessment of strength and frequency of meteotsunamis in future climate. Geophys. Res. Lett. 45, 10501–10508. https://doi.org/10.1029/2018GL079566.

Williams, D.A., Schultz, D.M., Horsburgh, K.J., Hughes, C.W., 2021. An 8-yr meteotsunami climatology across Northwest Europe: 2010-17. J. Phys. Oceanogr. 1145–1161. https://doi.org/10.1175/JPO-D-20-0175.1.

Yu, S., Ma, J., 2021. Deep learning for geophysics: current and future trends. Rev. Geophys. 59 (3) https://doi.org/10.1029/2021RG000742.

Zemunik, P., Bonanno, A., Mazzola, S., Giacalone, G., Fontana, I., Genovese, S., Basilone, G., Candela, J., Šepić, J., Vilibić, I., Aronica, S., 2021a. Observing meteotsunamis ("Marrobbio") on the southwestern coast of Sicily. Nat. Hazards 196, 1337–1363. https://doi.org/10.1007/s11069-020-04303-2.

Zemunik, P., Vilibić, I., Šepić, J., Pellikka, H., Ćatipović, L., 2021b. MISELA: 1-minute sea-level analysis global dataset. Earth Syst. Sci. Data 13, 4121–4132. https://doi.org/10.5194/essd-13-4121-2021.

Zemunik, P., Vilibić, I., Šepić, J., Pellikka, H., Ćatipović, L., 2021c. MISELA: minute sea-level analysis. Mar. Data Arch. https://doi.org/10.14284/456.

Zemunik, P., Denamiel, C., Šepić, J., Vilibić, I., 2022. High-frequency sea-level analysis: global distributions. Global Planet. Change 210, 103775. https://doi.org/10.1016/j.gloplacha.2022.103775.

Zhou, L., Lin, S.-J., Chen, J.-H., Harris, L.M., Chen, X., Rees, S.L., 2019. Toward convective-scale prediction within the next generation global prediction system. Bull. Am. Meteorol. Soc. 100 (7), 1225–1243. https://doi.org/10.1175/bams-d-17-0246.1.